CHEMISTRY OF MATERIALS
Article

Chem. Mater. **2010,** *22,* 4435–4445 4435
DOI:10.1021/cm101130a

A Combined Total Scattering and Simulation Approach to Analyzing Defect Structure in Bi_3YO_6

Isaac Abrahams,*[,†] Xi Liu,[†] Stephen Hull,[‡] Stefan T. Norberg,[‡,§] Franciszek Krok,[∥] Anna Kozanecka-Szmigiel,[∥] M. Saiful Islam,[⊥] and Stephen J. Stokes[⊥]

[†]*Centre for Materials Research, School of Biological and Chemical Sciences, Queen Mary University of London, Mile End Road, London E1 4NS, United Kingdom,* [‡]*ISIS Facility, Rutherford Appleton Laboratory, Chilton, Didcot, Oxon OX11 0QX, United Kingdom,* [§]*Department of Chemical and Biological Engineering, Chalmers University of Technology, SE-412 96 Gothenburg, Sweden,* [∥]*Faculty of Physics, Warsaw University of Technology, ul. Koszykowa 75, 00-662, Warsaw, Poland, and* [⊥]*Department of Chemistry, University of Bath, Bath BA2 7AY, United Kingdom*

Received April 22, 2010. Revised Manuscript Received June 24, 2010

The defect structure and electrical properties of the fast oxide ion-conducting solid electrolyte δ-Bi_3YO_6 have been studied using a combination of total neutron scattering analysis, energy minimization methods, and AC impedance spectroscopy. Conventional structural analysis using the Rietveld method reveals the oxide ions to be distributed over three crystallographic sites at room temperature, with a small change in this distribution at 800 °C. Analysis of short-range correlations using a total neutron scattering approach yields information on Bi and Y coordination environments. Careful analysis of the angular distribution functions derived from reverse Monte Carlo modeling of the total scattering data reveals physical evidence for a predominance of ⟨110⟩ vacancy ordering in this system. This ordering is confirmed as the lowest energy configuration in parallel energy minimization simulations.

1. Introduction

Many of the best anion-conducting solid electrolytes exhibit the fluorite structure and have applications in fuel cells, sensors, and oxygen pumps; well-known examples are yttrium-stabilized zirconia ($Zr_{1-x}Y_xO_{2-x/2}$, abbreviated as YSZ) and gadolinium-doped ceria ($Ce_{1-x}Gd_xO_{2-x/2}$, abbreviated as CGO).[1,2] The highest known oxide ion conductivity of any solid occurs in the defect fluorite δ-Bi_2O_3, with conductivities on the order of 1 S cm^{-1} at *ca.* 730 °C.[3] However, the stability window of this phase is rather limited and much research has been carried out with regard to stabilizing the high-temperature phase at substantially lower temperatures, mainly through solid-solution formation with other oxides.[4−8]

A variety of doped bismuth oxide phases have been isolated, some of which are closely related to the parent δ-Bi_2O_3. For example, the addition of Y_2O_3 to Bi_2O_3 has been shown to yield various phases.[3,9,10] The Bi_2O_3−Y_2O_3 binary system has been investigated by several authors, and their work has been extensively reviewed by Sammes et al.[7] The compound of composition Bi_3YO_6 shows particularly high oxide ion conductivity and was originally described as a pure δ-phase, stable at temperatures of <400 °C, by Datta and Meehan.[11] However, subsequent work by Watanabe's group[12−14] on compositions similar to that of Bi_3YO_6 suggests that, upon prolonged annealing at 650 °C, transformation of the δ-phase to a stable hexagonal phase occurs. This hexagonal phase converts rapidly back to the cubic phase at 720 °C and therefore they concluded that the room temperature δ-phase was formally a quenched metastable phase and that the kinetics of the cubic to hexagonal phase transition are very sluggish.

δ-Bi_3YO_6 is structurally very similar to δ-Bi_2O_3.[15,16] Y^{3+} being isovalent with Bi^{3+} results in the same nominal vacancy concentration in the yttrate as in the pure bismuth

*Author to whom correspondence should be addressed. Tel.: +44 207 882 3235. E-mail: i.abrahams@qmul.ac.uk.

(1) Steele, B. C. H. In *High Conductivity Solid Ionic Conductors*; Takahashi, T., Ed.; World Scientific: Singapore, 1989; p 402.
(2) Godickemeier, M.; Sasaki, K.; Gauckler, L. J. *J. Electrochem. Soc.* **1997**, *144*, 1635.
(3) Takahashi, T.; Iwahara, H.; Nagai, Y. *J. Appl. Electrochem.* **1972**, *2*, 97.
(4) Mairesse, G. In *Fast Ion Transport in Solids*; Scrosati, B., Magistris, A., Mari, C. M., Mariotto, G., Eds.; Kluwer Academic Publishers: Dordrecht, The Netherlands, 1993; p 271.
(5) Boivin, J. C.; Mairesse, G. *Chem. Mater.* **1998**, *10*, 2870.
(6) Shuk, P.; Wiemhöfer, H. D.; Guth, U.; Göpel, W.; Greenblatt, M. *Solid State Ionics* **1996**, *89*, 179.
(7) Sammes, N. M.; Tompsett, G. A.; Näfe, H.; Aldinger, F. *J. Eur. Ceram. Soc.* **1999**, *19*, 1801.
(8) Azad, A. M.; Larose, S.; Akbar, S. A. *J. Mater. Sci.* **1994**, *29*, 4135.
(9) Takahashi, T.; Iwahara, H.; Arao, T. *J. Appl. Electrochem.* **1975**, *5*, 187.
(10) Punn, R.; Feteira, A. M.; Sinclair, D. C.; Greaves, C. *J. Am. Chem. Soc.* **2006**, *128*, 15386.
(11) Datta, R. K.; Meehan, J. P. *Z. Anorg. Allg. Chem.* **1971**, *383*, 328.
(12) Watanabe, A.; Kikuchi, T. *Solid State Ionics* **1986**, *21*, 287.
(13) Watanabe, A. *Solid State Ionics* **1990**, *40/41*, 889.
(14) Watanabe, A. *Solid State Ionics* **1996**, *86−88*, 1427.
(15) Battle, P. D.; Catlow, C. R. A.; Drennan, J.; Murray, A. D. *J. Phys. C* **1983**, *16*, 561.
(16) Battle, P. D.; Catlow, C. R. A.; Heap, J. W.; Moroney, L. M. *J. Solid State Chem.* **1986**, *63*, 8.

Published on Web 07/19/2010

oxide (1/4 of the available oxide ion sites in the fluorite structure are vacant in both systems). However, there are likely to be significant differences associated with the preferred coordination environments of Bi^{3+} and Y^{3+}, as evidenced by EXAFS studies.[17] Detailed characterization of the defect structure in these systems is key to understanding the ionic conduction mechanism. Nevertheless, since these phases are disordered on the crystallographic scale, conventional diffraction methods yield only an average picture. Short-range ordering manifests itself in the diffuse scattering, which appears as background features in powder diffraction patterns. Typically, the diffuse scattering is ignored in the analysis of crystalline diffraction patterns. However, recent advances in total scattering analysis have allowed for the inclusion of these data to yield a more complete picture of the short-range structure.[18]

Several studies have been carried out on modeling the undoped δ-Bi_2O_3 structure, in particular to assess the vacancy ordering. Jacobs and MacDonaill[19−22] investigated various models and found that ⟨111⟩-aligned vacancies were more stable than those aligned along ⟨100⟩, but that ⟨110⟩ vacancies are also present. Total energy calculations by Medvedeva et al.[23] also found ⟨111⟩ vacancy ordering to be the most stable. These findings are in contrast to those of Walsh et al.,[24] who used density functional theory (DFT) calculations to predict that ⟨100⟩ ordering is favored. In a recent detailed investigation by Aidhy et al.,[25] using molecular dynamics (MD) and *ab initio* methods, it was concluded that a combination of ⟨110⟩ and ⟨111⟩ vacancy alignment occurs. Even more recent publications, utilizing a combination of DFT and neutron total scattering data by Mohn et al.[26] and Hull et al.,[27] have shown that δ-Bi_2O_3 does not adopt a fluorite structure at the local scale, but instead favors an asymmetric Bi^{3+} coordination that is closely related to that found in the metastable β-Bi_2O_3 phase. Using maximum entropy methods (MEM) with powder neutron diffraction data, Yashima and Ishimura[28] found experimental evidence for diffusion pathways in both the ⟨111⟩- and ⟨100⟩-directions. These diffusion pathways were also consistent with an MEM analysis of the doped system δ-$Bi_{1.4}Yb_{0.6}O_3$ by the same authors.[29] Previous studies of diffuse neutron scattering in the bismuth yttrate fluorites were consistent with anion vacancy ordering in ⟨111⟩ and ⟨110⟩ directions.[16]

There are relatively few studies involving a combination of structural and computer modeling of doped bismuth oxides. Here, we present the results of a total scattering analysis of defect structure in δ-Bi_3YO_6, utilizing both Bragg and diffuse scattering, combined with energy minimization calculations, to give a more complete picture of the short-range ordering in this system.

2. Experimental Section

2.1. Sample Preparations. Samples of Bi_3YO_6 were prepared using appropriate amounts of Bi_2O_3 (Aldrich, 99.9%) and Y_2O_3 (Aldrich, 99.99%). Starting mixtures were ground in methylated spirits on a McCrone micronizing mill for 30 min. The dried mixtures were heated initially at 740 °C for 24 h, then cooled and reground. Powders were then reheated at 850 °C for 24 h and quenched in air to room temperature. For electrical measurements, reacted powders were pressed isostatically at a pressure of 400 MPa, then sintered at 800 °C for 10 h, before slow cooling in air to room temperature over a period of ∼12 h. Phase purity was confirmed by powder X-ray diffraction (XRD), as described below.

2.2. Electrical Measurements. Electrical parameters were determined by AC impedance spectroscopy up to *ca.* 800 °C, using a fully automated Solartron Model 1255/1286 system in the frequency range from 1 Hz to 5×10^5 Hz. Samples for impedance measurements were prepared as rectangular blocks (*ca.* 6 mm × 3 mm × 3 mm) cut from slow-cooled sintered pellets, using a diamond saw. Platinum electrodes were sputtered by cathodic discharge. Impedance spectra were recorded over two cycles of heating and cooling at stabilized programmed temperatures. Impedance at each frequency was measured repeatedly until consistency (2% tolerance in drift) was achieved or a maximum number of 25 repeats had been reached, as previously described.[30]

2.3. Crystallography. Powder XRD data were collected at room temperature and at 800 °C on a PANalytical X'Pert Pro diffractometer fitted with an X'Celerator detector, using nickel-filtered Cu Kα radiation (λ_1 = 1.54056 Å and λ_2 = 1.54439 Å) with an Anton-Paar HTK-15 high-temperature camera. Calibration was carried out with an external Si standard. Data were collected in flat plate θ/θ geometry over the 2θ range of 5°−120°, in steps of 0.033°, with a scan time of 200 s per step.

Powder neutron diffraction data were collected on the Polaris diffractometer at the ISIS facility located at the Rutherford Appleton Laboratory.[31] Data were collected on backscattering (130°−160°), 90° (85°−95°), low-angle (28°−42°), and very low angle (13°−15°) detectors. For the room-temperature total scattering experiment, the sample was contained in a cylindrical 11-mm-diameter vanadium can located in front of the backscattering detectors and a dataset of 1000 μA h collected. For the standard elevated temperature measurements, a sample was placed in an 11-mm-diameter vanadium can and placed in an evacuated furnace in front of the backscattering detectors. Short

(17) Battle, P. D.; Catlow, C. R. A.; Chadwick, A. V.; Cox, P.; Greaves, G. N.; Moroney, L. M. *J. Solid State Chem.* **1987**, *69*, 230.
(18) Keen., D. A. *J. Appl. Crystallogr.* **2001**, *34*, 172.
(19) Jacobs, P. W. M.; MacDonaill, D. A. *Solid State Ionics* **1986**, *18&19*, 209.
(20) Jacobs, P. W. M.; MacDonaill, D. A. *Solid State Ionics* **1987**, *23*, 279.
(21) Jacobs, P. W. M.; MacDonaill, D. A. *Solid State Ionics* **1987**, *23*, 295.
(22) Jacobs, P. W. M.; MacDonaill, D. A. *Solid State Ionics* **1987**, *23*, 307.
(23) Medvedeva, N. I.; Zhukov, V. P.; Gubanov, V. A.; Novikov, D. L.; Klein, M. L. *J. Phys. Chem. Solids* **1996**, *57*, 1243.
(24) Walsh, A.; Watson, G. W.; Payne, D. J.; Edgell, R. G.; Guo, J.; Glans, P.-A.; Learmont, T.; Smith, K. E. *Phys. Rev. B.* **2006**, *73*, 235104.
(25) Aidhy, D. S.; Nino, J. C.; Sinnott, S. B.; Wachsman, E. D.; Phillpot, S. R. *J. Am. Ceram. Soc.* **2008**, *91*, 2349.
(26) Mohn, C. E.; Stølen, S.; Norberg, S. T.; Hull, S. *Phys. Rev. Lett.* **2009**, *102*, 155502.
(27) Hull, S.; Norberg, S. T.; Tucker, M. G.; Eriksson, S. G.; Mohn, C. E.; Stølen, S. *Dalton Trans.* **2009**, 8737.
(28) Yashima, M.; Ishimura, D. *Chem. Phys. Lett.* **2003**, *378*, 395.
(29) Yashima, M.; Ishimura, D. *Appl. Phys. Lett.* **2005**, *87*, 221909.
(30) Dygas, J. R.; Kurek, P.; Breiter, M. W. *Electrochim. Acta* **1995**, *40*, 1545.
(31) Hull, S.; Smith, R. I.; David, W. I. F.; Hannon, A. C.; Mayers, J.; Cywinski, R. *Physica B* **1992**, *180−181*, 1000.

data collections of 30 μA h were made at temperatures from 300 °C to 800 °C, to allow for assessment of lattice expansion. For the total scattering study at 800 °C, a sample was sealed in an evacuated silica glass tube (8 mm diameter) and placed inside an 11-mm-diameter vanadium can inside an evacuated furnace in front of the backscattering detectors. An extended data collection of 1000 μA h was carried out at this temperature. For the total scattering analysis data corrections, diffraction data were collected on an empty silica tube inside a vanadium can for a similar time and under identical conditions to the sample. In addition, measurements of the empty furnace and a vanadium rod at room temperature were made, with the latter used to correct for the wavelength dependence of the incident neutron flux.

3. Data Analysis and Computer Simulations

3.1. Rietveld Analysis. Average structure refinement was carried out by conventional Rietveld analysis with the General Structure Analysis System (GSAS) suite of programs,[32] using a combination of X-ray and neutron datasets. A cubic model in space group $Fm\bar{3}m$ was used for all refinements. Bi and Y were located on the ideal 4*a* site (0,0,0) with oxide ions distributed over three sites: 8*c* at (0.25, 0.25, 0.25), 32*f* at approximately (0.3, 0.3, 0.3) and 48*i* at around (0.5, 0.2, 0.2).[33] For the data collected at 800 °C, the diffraction pattern of an empty silica tube was subtracted prior to refinement.

3.2. Total Neutron Scattering Analysis. Neutron diffraction datasets collected for Bi_3YO_6 at room temperature and at 800 °C were used in reverse Monte Carlo (RMC)[34] simulations to probe the instantaneous local ordering in the crystal structure. The effects of background scattering and beam attenuation were corrected for using the program Gudrun[35] and the resulting normalized total scattering structure factors, $S(Q)$ (where Q is the scattering vector defined as $2\pi/d$), were then used to obtain the corresponding total radial distribution function, $G(r)$, via Fourier transformation. The analysis of the total neutron scattering data (Bragg peaks plus diffuse scattering components) was carried out using the RMCProfile software.[36] All RMC simulations used configuration boxes of $10 \times 10 \times 10$ unit cells, containing a total of 3000 Bi, 1000 Y, and 6000 O atoms. The initial model was based on the ideal fluorite structure with cations and anions randomly distributed over sites in the supercell corresponding to the regular 4*a* and 8*c* crystallographic sites, respectively, in the cubic $Fm\bar{3}m$ subcell. Fitting was carried out against the reciprocal space data, $S(Q)$, the real space data, $G(r)$, and the Bragg profile data, with the latter used to provide a constraint for the long-range crystallinity. The former was broadened by convolution with a box function to reflect the finite size of the simulation box:

$$S_{\mathrm{box}}(Q) = \frac{1}{\pi}\int_{-\infty}^{\infty} S_{\mathrm{expt}}(Q')\frac{\sin L(Q-Q')/2}{Q-Q'}\,\mathrm{d}Q' \quad (1)$$

where L is the smallest dimension of the RMC configuration and, as such, defines the upper limit of $G(r)$. Further details on the total scattering method have been described by Tucker et al.[36]

Calculations were performed using bond valence summation (BVS) constraints[37] and an O−O closest approach constraint ($g_{\mathrm{OO}}(r)$) to avoid unrealistically short O−O contacts. The BVS parameters used for the soft BVS constraint were all taken from Brese and O'Keeffe.[38] Cation swapping (one random cation swapping positions with a random cation of another atomic species) was tested and found to have no significant influence on the fit. Therefore, in the final calculations, only translational moves were permitted. The final fits to the $S_{\mathrm{box}}(Q)$ and $G(r)$ data for Bi_3YO_6 at room temperature and at 800 °C are shown in Figure 1.

3.3. Energy Minimization Simulations. The simulations were formulated within the framework of the Born model, the main features of which are the nature of the interatomic potentials and the description of perfect and defective lattices. The present account of these techniques will be brief, since comprehensive reviews have been given elsewhere.[39−42] The interactions between the ions were calculated taking into account long-range Coulombic forces and short-range forces that account for electron cloud overlap (Pauli repulsion) and dispersion (van der Waals) interactions. The short-range interactions were modeled with a Buckingham interatomic potential:

$$\phi_{\alpha\beta}(r) = \frac{Z_\alpha Z_\beta e^2}{4\pi\varepsilon_0 r} + A_{\alpha\beta}\exp\left(-\frac{r}{\rho_{\alpha\beta}}\right) - \frac{C_{\alpha\beta}}{r^6} \quad (2)$$

where $A_{\alpha\beta}$, $\rho_{\alpha\beta}$, and $C_{\alpha\beta}$ are potential parameters assigned to each ion−ion interaction; r is the distance between ions α and β, and Z_α and Z_β are their respective charges. The lattice energy calculations employ the now-standard Ewald summation procedures for the Coulombic interactions. Polarizability of the ions, which is an important parameter, especially for a lone-pair cation, was incorporated using the Dick−Overhauser[43] shell model.

An important feature of the calculations is the treatment of lattice relaxation about the point defect or dopant of interest. The Mott−Littleton approach used here involves the partitioning of the crystal lattice into two regions, so

(32) Larson, A. C.; Von Dreele, R. B. General Structure Analysis System; Los Alamos National Laboratory Report LAUR 8-748; Los Alamos National Laboratory: Los Alamos, NM, **1986**.
(33) Abrahams, I.; Kozanecka-Szmigiel, A.; Krok, F.; Wrobel, W.; Chan, S. C. M.; Dygas, J. R. *Solid State Ionics* **2006**, *177*, 1761.
(34) McGreevy, R. L. *J. Phys.: Condens. Matter* **2001**, *13*, R877.
(35) Soper, A. K. Unpublished software.
(36) Tucker, M. G.; Keen, D. A.; Dove, M. T.; Goodwin, A. L.; Hui, Q. *J. Phys.: Condens. Matter* **2007**, *19*, 335218.
(37) Norberg, S. T.; Tucker, M. G.; Hull, S. *J. Appl. Crystallogr.* **2009**, *42*, 179.
(38) Brese, N. E.; O'Keeffe, M. *Acta Crystallogr., Sect. B: Struct. Sci.* **1991**, *B47*, 192.
(39) Catlow, C. R. A.; Mackrodt, W. C. *Computer Simulation of Solids, Lecture Notes in Physics*; Springer: Berlin, 1982.
(40) Catlow, C. R. A. In *Solid State Chemistry-Techniques*; Cheetham, A. K., Day, P., Eds.; Clarendon Press: Oxford, U.K., 1987; p 231.
(41) Catlow, C. R. A. *Computer Modelling in Inorganic Crystallography*; Academic Press: San Diego, CA, 1997.
(42) Woodley, S. M.; Catlow, C. R. A. *Nat. Mater.* **2008**, *7*, 937.
(43) Dick, B. G.; Overhouser, A. W. *Phys. Rev.* **1958**, *112*, 90.

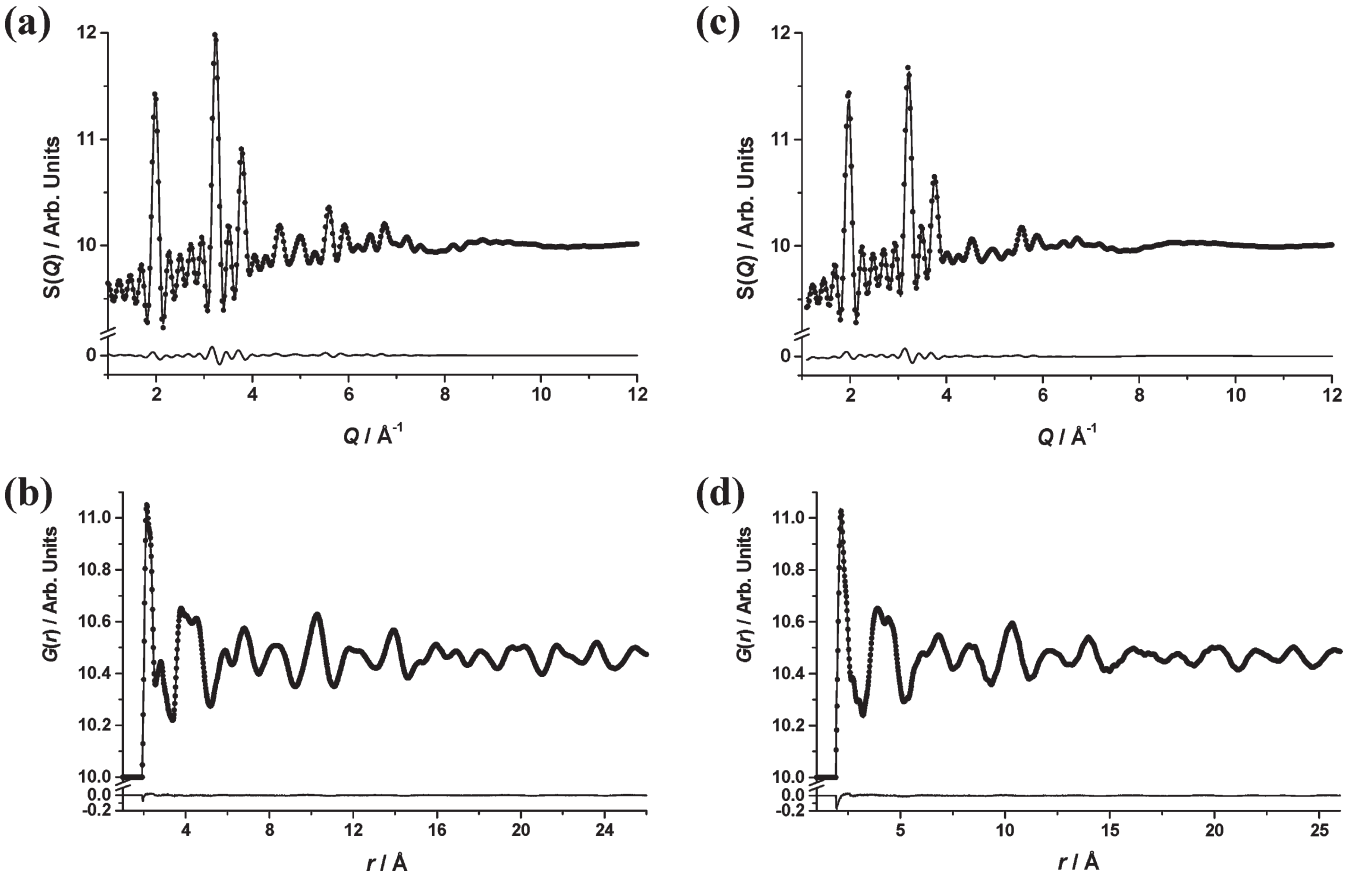

Figure 1. (a and c) Fitted total scattering $S(Q)$ and (b and d) total radial distribution $G(r)$ functions for Bi_3YO_6 at 25 °C (panels (a) and (b)) and 800 °C (panels (c) and (d)). Observed (points), calculated (line), and difference (lower) profiles are shown.

that ions within the spherical inner region surrounding the defect are relaxed explicitly. The remainder of the crystal, where the defect forces are relatively weak, are treated by more approximate quasi-continuum methods. In this way, local relaxation about the defect or impurity was effectively modeled and the crystal was not considered simply as a rigid lattice. These methods are embodied in the GULP simulation code,[44] and the techniques have been applied successfully to a range of materials including other bismuth-based oxides such as Bi_2WO_6 and $Bi_4Ti_3O_{12}$.[45−47]

Short-range parameters for Bi−O and Bi−Bi interactions and shell model parameters for each ion were taken directly from a previous study on Bi_2WO_6,[46] while the parameters of Y−O were taken from a study of binary and ternary oxides.[48] The parameters for the O−O interaction were obtained from work by Grimes et al.[49] The full set of interatomic potentials and shell model parameters used in the present study are listed in Table 1. For the present calculations, a supercell 27 times the size of the fluorite unit cell was constructed in space group $P1$, so that all atom sites within the cell could serve as locations for point defects. In creating this system, the anions were positioned only at the ideal fluorite anion site (8*c* in space group $Fm\bar{3}m$), to keep the occupancy of anion sites as simple as possible. Repetition of the unit cell in three dimensions ensured that the Y atoms were evenly distributed throughout the crystal lattice with maximum separation.

Table 1. Interatomic Potential and Shell Model Parameters Used for Bi_3YO_6

(a) Short-Range

interaction	A (eV)	ρ (Å)	C (eV Å^6)
$Bi^{3+}\cdots Bi^{3+}$	24244.5	0.3284	0
$Bi^{3+}\cdots O^{2-}$	49529.35	0.2223	0
$O^{2-}\cdots O^{2-}$	9547.96	0.2192	32
$Y^{3+}\cdots O^{2-}$	1519.279	0.3291	0

(b) Shell Model

species	shell charge (e)	force constant (eV Å^{-2})
Bi^{3+}	−5.51	359.55
O^{2-}	−2.04	6.3

4. Results and Discussion

4.1. Electrical Conductivity. The Arrhenius plot of total conductivity for Bi_3YO_6 is shown in Figure 2. The

(44) Gale, J. D. *J. Chem. Soc., Faraday Trans.* **1997**, *93*, 629.
(45) Pirovano, C.; Islam, M. S.; Vannier, R. N.; Nowogrocki, G.; Mairesse, G. *Solid State Ionics* **2001**, *140*, 115.
(46) Islam, M. S.; Lazure, S.; Vannier, R. N.; Nowogrocki, G.; Mairesse, G. *J. Mater. Chem.* **1998**, *8*, 655.
(47) Snedden, A.; Lightfoot, P.; Dinges, T.; Islam, M. S. *J. Solid State Chem.* **2004**, *177*, 3660.
(48) Bush, T. S.; Gale, J. D.; Catlow, C. R. A.; Battle, P. D. *J. Mater. Chem.* **1994**, *4*, 831.
(49) Grimes, R. W.; Busker, G.; McCoy, M. A.; Chroneos, A.; Kilner, J. A. *Ber. Bunsen. Phys. Chem.* **1997**, *101*, 1240.

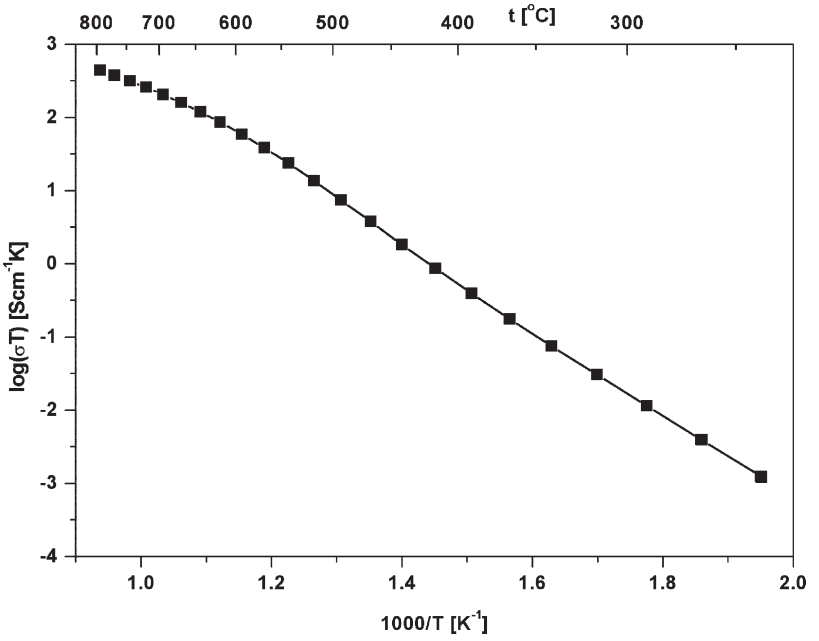

Figure 2. Arrhenius plot for total conductivity in Bi_3YO_6. Data corresponding to the second cooling cycle are shown.

conductivity data were fully reproducible on heating and cooling cycles, and those data corresponding to the second cooling cycle are shown. The plot can be interpreted as containing two linear regions: one at low temperature and one at high temperature, with a large transition region between *ca.* 425 °C and 650 °C. The activation energy in the high-temperature region ($\Delta E_{HT} = 0.67 \pm 0.02$ eV) is significantly lower than that at low temperatures ($\Delta E_{LT} = 1.19 \pm 0.01$ eV). Conductivities in the two regions characterized by the conductivity at 300 °C and 700 °C (σ_{300} and σ_{700}, respectively) are 3.7×10^{-5} S cm^{-1} and 2.7×10^{-1} S cm^{-1}, respectively, and confirm excellent conductivity for this phase, as previously reported.[33,50]

4.2. Average Structure of Bi_3YO_6. Figure 3 shows the diffraction profiles for Bi_3YO_6 at 25 and 800 °C, fitted using conventional Rietveld analysis, with the corresponding crystal and refinement parameters in Table 2. The refined structural parameters are summarized in Table 3, with significant contact distances given in Table 4. All Bragg peaks can be indexed on the $Fm\bar{3}m$ cubic cell and the absence of superlattice reflections confirms that there is no long-range ordering of either anions or cations at both the studied temperatures. On the crystallographic scale, the oxide ions are found to be distributed over three sites in the $Fm\bar{3}m$ cell, viz, the 8*c*, 32*f*, and 48*i* sites (O(1), O(2), and O(3), respectively). The fractional coordinates of the three oxide ion sites are in good agreement with those reported previously,[15,16] although the distribution of scattering between these sites varies somewhat. In addition, the average position for the cation site in the present study is found to lie very close to the ideal 4*a* site, rather than the slightly shifted 24*e* site refined in the previous studies. Only the 32*f* and 8*c* sites are found to be occupied in the parent compound δ-Bi_2O_3,[15,27,28,51−53] and it is therefore reasonable to suppose that oxide ions in the 48*i* site are exclusively associated with coordination to yttrium. Indeed, the location of the 48*i* site allows for a distorted octahedral coordination for the Y^{3+} cations (see Figure 4).

There is clear nonlinearity in the thermal variation of the cubic lattice parameter (see Figure 5), with the unit cell parameter being ~0.5% larger at 800 °C than would be expected from a simple linear expansion of the lattice. This is a common feature in substituted bismuth oxide-based fluorites.[7] There are no obvious changes in the diffraction patterns (Figure 3), which suggests that the observed nonlinear behavior may be associated with a subtle second-order transition. The thermal variation of the cation and anion isotropic thermal parameters is shown in Figure 6. The cation thermal parameter is closely correlated to the thermal expansion of the lattice parameter and is clearly dominated by thermal vibration. Similarly, the thermal variation of the anion thermal parameter reflects that of the cubic lattice parameter, but it is also significantly larger than that for the cations, because it describes significant disorder on the oxide ion sites, as well as thermal vibration.

At 800 °C, there is little significant change in the oxide ion distribution, compared to that at room temperature. Only the occupancy of the 48*i* site (O(3)) increases significantly (*ca.* 55%) at 800 °C, coupled with a 4% increase in the M−O(3) distance compared to modest rises of *ca.* 1% for M−O(2) and M−O(1) (Table 4). The increase in the 48*i* site occupancy appears to occur mainly at the expense of that of the 8*c* site (O(1)), although the value of the 8*c* site occupancy at 800 °C lies within two estimated standard deviations of the value at room temperature; therefore, the change cannot be regarded as

(50) Takahashi, T.; Iwahara, H. *Mater. Res. Bull.* **1978**, *13*, 1450.
(51) Gattow, G.; Schroeder, H. *Z. Anorg. Allg. Chem.* **1962**, *318*, 176.
(52) Hund, F. *Z. Anorg. Allg. Chem.* **1964**, *333*, 248.
(53) Harwig, H. A. *Z. Anorg. Allg. Chem.* **1978**, *444*, 151.

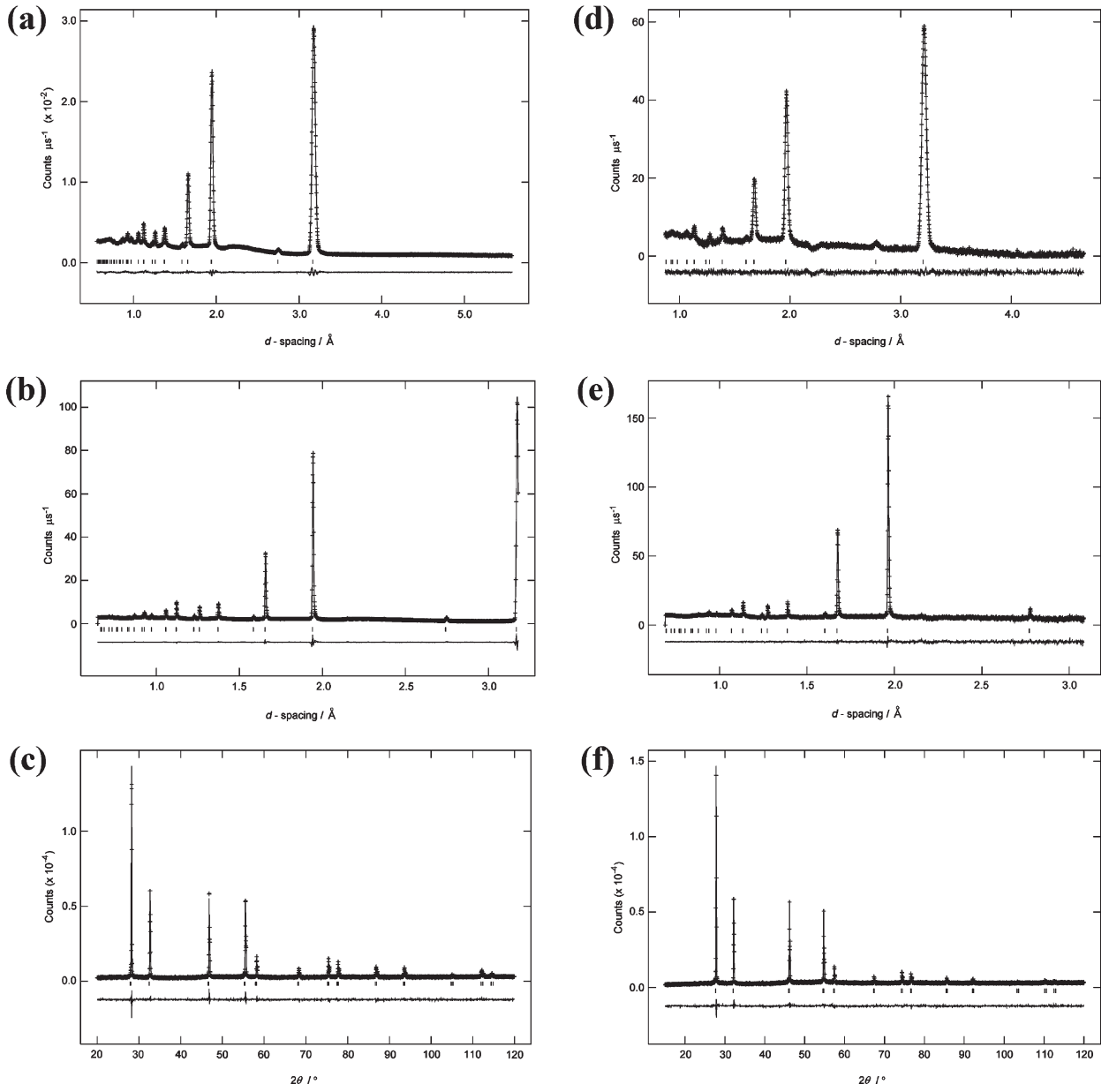

Figure 3. Diffraction profiles for Bi_3YO_6 at (a−c) 25 °C and (d−f) 800 °C, fitted using the Rietveld method. Observed (denoted by cross (+) symbols), calculated (denoted as a solid line), and difference (lower) profiles are shown with reflection positions indicated by markers. Neutron low-angle (panels (a) and (d)), neutron backscattering (panels (b) and (e)), and X-ray (panels (c) and (f)) data are shown.

significant. The observed change in 48*i* site occupancy may be used to explain the nonlinear thermal expansion of the cubic lattice parameter by considering ions on the site to be the interstitial of a Frenkel defect. As the occupancy of this site increases, one would expect an increase in the local distortion of the lattice, translating to a larger lattice parameter than that which would be expected from a simple thermal expansion. Although the increase in Frenkel defects must generate a higher vacancy concentration on the fluorite oxide ion sites (either 32*f* or 8*c*), these additional vacancies are effectively trapped in the yttrium coordination sphere; therefore, this increase in Frenkel defect concentration effectively reduces charge carrier concentration with a resultant reduction in conductivity.

4.3. Short-Range Structure. Bond valence sums from the RMC calculations yielded average valences for Bi, Y, and O of +3.08, +2.98, and −2.03 at room temperature and +2.99, +2.98, and −1.99 at 800 °C, respectively. Selected pair correlation functions for Bi_3YO_6 at 25 °C and at 800 °C are shown in Figure 7. Apart from the expected thermal shift, there is very little obvious difference between the individual pair correlations at the two studied temperatures.

Figure 8 shows the distribution of contact distances around bismuth and yttrium. Using the first minimum in the $g_{ij}(r)$ pair correlation function as a cutoff, the mode Bi−O and Y−O contact distances were found to be 2.456 Å and 2.425 Å at room temperature and 2.362 Å and 2.279 Å at 800 °C, respectively, yielding Bi−O and Y−O coordination numbers of 6.05 and 6.31 at 25 °C and 5.30 and 5.29 at 800 °C, respectively. The structural model resulting from the RMC calculations was analyzed to

Table 2. Crystal and Refinement Parameters for Long-Range Structure of Bi_3YO_6 at 25 and 800 °C

chemical formula	Bi_3YO_6	Bi_3YO_6
formula weight	811.84 g mol^{-1}	811.84 g mol^{-1}
temperature	25 °C	800 °C
crystal system	cubic	cubic
space group	$Fm\bar{3}m$	$Fm\bar{3}m$
unit cell dimension	a = 5.49458(9) Å	a = 5.55982(7) Å
volume	165.884(8) Å^3	171.863(7) Å^3
Z	1	1
density (calculated)	8.127 Mg cm^{-3}	7.844 Mg cm^{-3}
sample description	yellow powder	yellow powder
R-factors[a]		
(a) X-ray		
R_p	0.0573	0.0584
R_{wp}	0.0754	0.0738
R_{ex}	0.0462	0.0536
R_F^2	0.0841	0.0991
(b) Neutron backscattering		
R_p	0.0183	0.0425
R_{wp}	0.0152	0.0227
R_{ex}	0.0039	0.0241
R_F^2	0.1509	0.0462
(c) Neutron low angle		
R_p	0.0189	0.0571
R_{wp}	0.0241	0.0423
R_{ex}	0.0112	0.0515
R_F^2	0.1218	0.0279
total number of variables	118	118
number of profile points used		
X-ray	2990	3134
neutron backscattering	3302	2996
neutron low angle	4082	3261

[a] For definitions of the R-factors, see ref 32.

Table 3. Refined Parameters for Long-Range Structure of Bi_3YO_6 at (a) 25 and (b) 800 °C

(a) @ 25 °C

atom	site	x	y	z	Occ	U_{iso} (Å^2)
Bi	4a	0.0	0.0	0.0	0.75	0.0436(1)
Y	4a	0.0	0.0	0.0	0.25	0.0436(1)
O(1)	8c	0.25	0.25	0.25	0.391(5)	0.0606(4)
O(2)	32f	0.3076(6)	0.3076(6)	0.3076(6)	0.074(1)	0.0606(4)
O(3)	48i	0.5	0.1920(12)	0.1920(12)	0.011(1)	0.0606(4)

(b) @ 800 °C

atom	site	x	y	z	Occ	U_{iso} (Å^2)
Bi	4a	0.0	0.0	0.0	0.75	0.0687(3)
Y	4a	0.0	0.0	0.0	0.25	0.0687(3)
O(1)	8c	0.25	0.25	0.25	0.388(27)	0.080(2)
O(2)	32f	0.3089(23)	0.3089(23)	0.3089(23)	0.073(5)	0.080(2)
O(3)	48i	0.5	0.1656(13)	0.1656(13)	0.017(1)	0.080(2)

Table 4. Significant Contact Distances in Bi_3YO_6 at 25 and 800 °C

	Contact Distance (Å)	
bond	25 °C	800 °C
Bi/Y−O(1)	2.37922(3)	2.40747(3)
Bi/Y−O(2)	2.2565(6)	2.282(2)
Bi/Y−O(3)	1.994(2)	2.075(4)

determine further details of local coordination environments. M−O bond distances were evaluated based on the sum of the ionic radii (with radii of 1.17, 1.089, and 1.38 Å for Bi^{3+}, Y^{3+}, and O^{2-}, respectively[54]). This approach allows for the exclusion of nonbonded interactions, particularly in the case of coordination to Bi, where the nonbonding $6s^2$ pair of electrons result in stereochemically distorted environments around Bi. Figure 9 shows a plot of the averages of the first eight contacts around bismuth and yttrium at the two studied temperatures. The plots are clearly sigmoidal in character, and the point of inflection corresponds to the change between bonding and nominally nonbonding interactions. This change is seen to occur between the fourth and fifth contacts for bismuth and at the fifth contact for yttrium at both temperatures, corresponding to Bi−O distances of 2.59 and 2.60 Å at room temperature and 800 °C, respectively, and 2.60 and 2.64 Å for Y−O at these two temperatures, respectively. The values for Bi−O are close to the sum of the respective ionic radii; however, the values for Y−O are considerably larger (2.55 Å for Bi−O and 2.40 Å for Y−O), indicating significant distortion of the Y−O polyhedra. Using these values as the maximum bond length criteria, the resulting mean bond lengths were found to be 2.261 and 2.212 Å at 25 °C and 2.268 and 2.219 Å at 800 °C for Bi−O and Y−O, respectively. The average coordination numbers, using these bonding criteria, were determined to be 4.28 and 4.66 at 25 °C and 4.38 and 4.74 at 800 °C for bismuth and yttrium, respectively.

In the case of bismuth, these values are consistent with stereochemical activity of the $6s^2$ electrons resulting in lower coordination geometries, while the values for yttrium are lower than expected. This is almost certainly due to the relatively poor neutron scattering contrast between yttrium and bismuth, with the higher coordination number of yttrium resulting from the bond-valence constraints rather than discernible differences in the scattering data. Interestingly, ^{89}Y NMR studies on this compound,[55] show a single broad resonance characteristic of a wide range of environments for Y.

There is little difference between the room temperature and 800 °C results other than an increase in the average bond lengths and a small increase in the coordination numbers. This suggests that the overall structure is relatively unchanged.

The average O−M site coordination number is 3.991 at room temperature and 3.628 at 800 °C, using the first minimum in the $g_{ij}(r)$ pair correlation function as a cutoff. These values are slightly lower than the ideal fluorite value of 4 and reflect the fact that a significant number of oxide ions are displaced into positions corresponding to the 48i site (O(3)) in the crystallographic model. The lower value at 800 °C is in agreement with the average structure refinements, which showed a significant increase in the occupancy of the 48i site. Using the maximum bond length criteria described above, the average O−M coordination numbers drop to 3.26 and 3.29 at 25 and 800 °C, respectively. These values now reflect more accurately the crystallographic model, which shows

(54) Shannon, R. D. *Acta Crystallogr., Sect. A: Cryst., Phys., Diffr., Theor. Gen. Crystallogr.* **1976**, *A32*, 751.

(55) Battle, P. D.; Montez, B.; Oldfield, E. *J. Chem. Soc. Chem. Commun.* **1988**, 584.

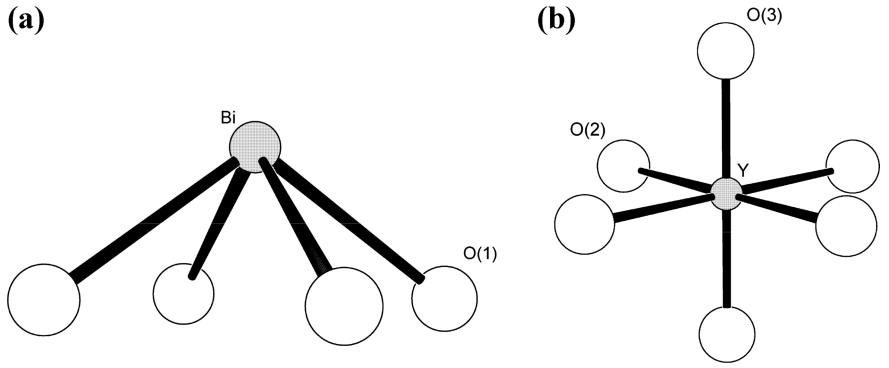

Figure 4. Proposed coordination geometries around (a) Bi and (b) Y in Bi_3YO_6, based on the average structure at 25 °C.

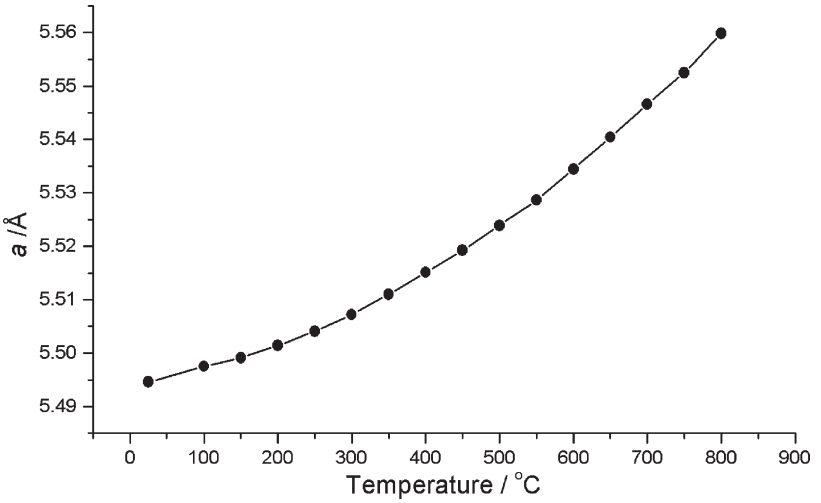

Figure 5. Thermal variation of cubic lattice parameter (a) in Bi_3YO_6. Estimated standard deviations are smaller than the symbols.

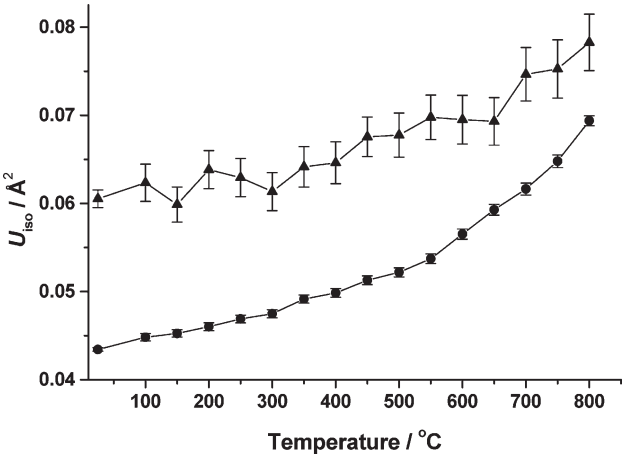

Figure 6. Thermal variation of (●) cation and (▲) anion isotropic thermal parameters in Bi_3YO_6. Error bars correspond to $\pm 2\sigma$ (where σ is the estimated standard deviation).

significant occupancy of the 32*f* site (O(2)). Oxygen atoms on this site are bonded to three metal atoms only.

The O−M−O angular distribution functions (ADFs) for Bi_3YO_6 at room temperature and at 800 °C are shown in Figure 10. Three maxima are observed, which can be explained by considering the cation coordination in the ideal fluorite structure (see Figure 11a). If one considers the cubic coordination around a single cation in the fluorite structure, there are three different O−M−O angles of 70°, 109°, and 180°. The relative numbers of each of these angles are in the ratio 6:6:2 and correspond to O−M−O angles between pairs of O atoms located on an edge, face, and body diagonal, respectively. In δ-Bi_2O_3, 1/4 of the oxide ion sites are vacant, which means the average bismuth coordination number is 6 in the ideal model, i.e., each Bi atom has two oxide ion vacancies in its coordination environment. As described above, the ordering of these vacancies has been the subject of much research with conflicting results.[19−25] The vacancies can be aligned randomly, in which case the ideal 6:6:2 ratio would be unaffected, or be aligned in ⟨111⟩-, ⟨100⟩-, or ⟨110⟩-directions, resulting in various ratios. Figure 11 summarizes the predicted angular distribution ratios for different vacancy ordering models in δ-Bi_2O_3.

The situation in δ-Bi_3YO_6 is somewhat different, because there is finite occupancy of the 48*i* site (O(3)) and a significant occupation of the 32*f* site (O(2)), which means that the system is far from the ideal case. If one considers the oxide ions located on the 48*i* site to be Frenkel interstitials, then the number of vacancies in the fluorite anion site (considered to be a combination of 8*c* and 32*f* sites) is closer to three vacancies around each metal atom. Again, several models can be proposed to describe the distribution of three vacancies (Figure 12).

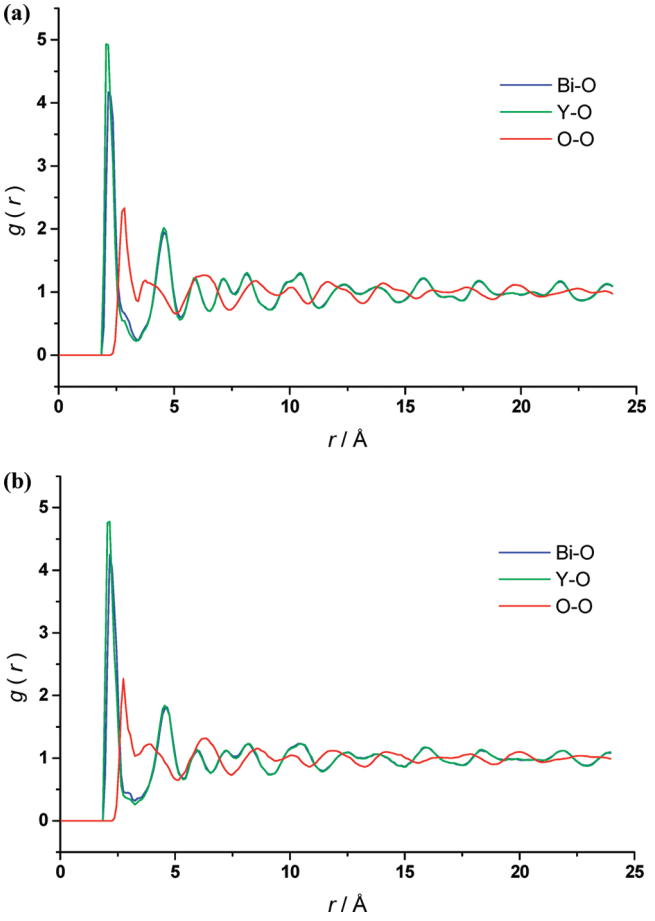

Figure 7. Selected pair correlation functions $g_{ij}(r)$ for Bi_3YO_6 at (a) 25 and (b) 800 °C.

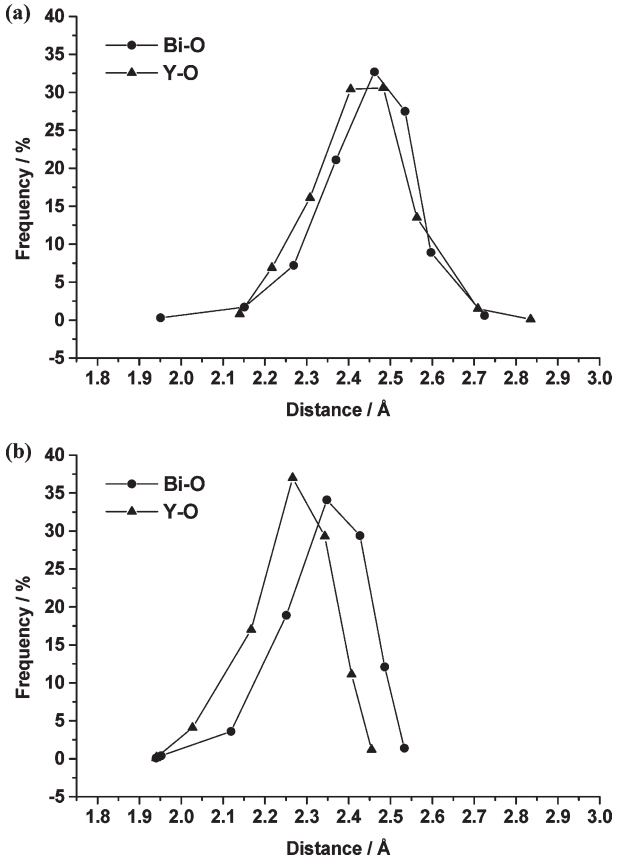

Figure 8. Contact distance distribution in Bi_3YO_6 at (a) 25 and (b) 800 °C.

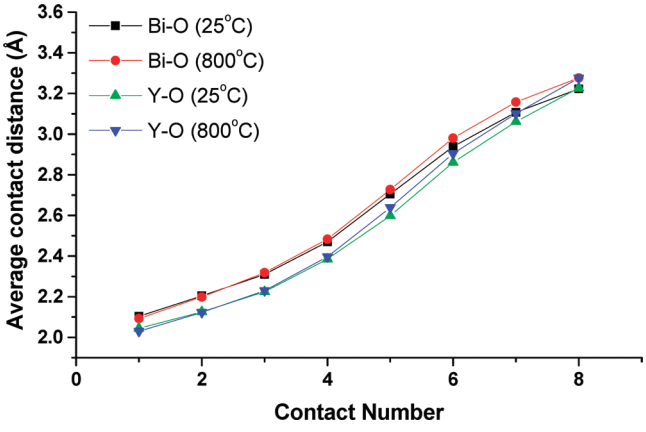

Figure 9. Average contact distances for the first eight contacts around the metal cations in Bi_3YO_6.

The peak positions of the O−M−O ADFs (Figure 10) represent the average angles over the peak ranges. The integrals of the functions over the angles from 0° to 180° give the angle ratio in each model, as summarized in Table 5. The observed values at room temperature clearly appear to be consistent with a predominantly ⟨110⟩ (or ⟨110⟩⟨011⟩) distribution of 2−3 vacancies around each metal atom. The 800 °C data show a significant increase in the middle angle, with respect to the other two angles. This is consistent with the observed increase in the 48*i* occupancy at this temperature. Again, the data are consistent with predominantly ⟨110⟩ ordering of vacancies.

4.4. Energy Minimization and Defect Simulations. As noted, large supercells of composition Bi_3YO_6 were examined by atomistic simulation methods to complement the structural studies. Energy minimization (structural optimization) of the oxygen vacancy ordering configurations shown in Figure 11 was carried out.

Comparison of the lattice energies of the ordering models listed in Table 6 reveals that ⟨111⟩ ordering is the least stable, with the ⟨110⟩ configuration slightly lower in energy than the ⟨100⟩ configuration and the disordered state. This is consistent with the structural analysis, indicating evidence for ⟨110⟩ vacancy ordering in δ-Bi_3YO_6. It is worth noting that previous *ab initio* studies of similar intrinsic oxygen vacancy ordering in pure δ-Bi_2O_3 found that ⟨111⟩ ordering was least favorable and ⟨100⟩ ordering was only 0.06 eV more stable than that of ⟨110⟩ ordering.[24] Furthermore, a more intensive molecular dynamics and *ab initio* study of pure δ-Bi_2O_3 by Aidhy et al.[25] found similar results, but also included an ordered 2 × 2 × 2 supercell, suggested by Boyapati et al.,[56] that contained a combination of ⟨111⟩ and ⟨110⟩ vacancy ordering.

The calculated unit cell parameters for Bi_3YO_6 for the different ordering models shown in Figure 11 are also

(56) Boyapati, S.; Wachsman, E. D.; Jiang, N. *Solid State Ionics* **2001**, *140*, 149.

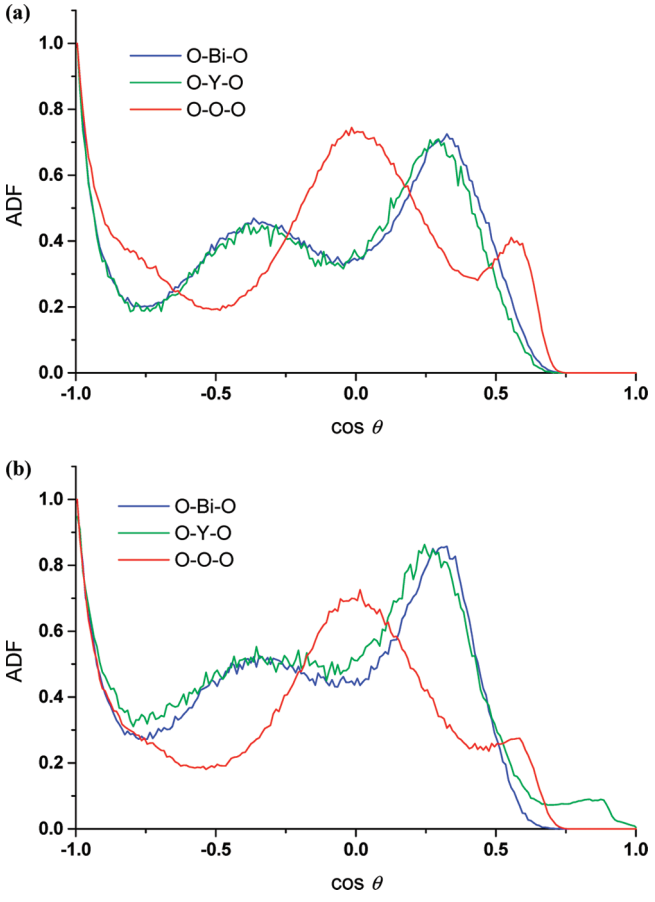

Figure 10. O−M−O angular distribution functions for Bi_3YO_6 at (a) 25 and (b) 800 °C.

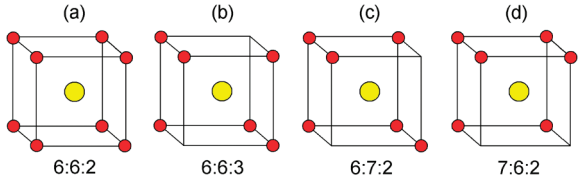

Figure 11. Models for oxide ion vacancy ordering in the idealized structure of δ-Bi_2O_3, showing (a) ideal fluorite, (b) ⟨111⟩, (c) ⟨110⟩, and (d) ⟨100⟩ ordering. Angle ratios for 70°, 109°, and 180° angles are given. Bi and O are indicated by large yellow and small red circles, respectively.

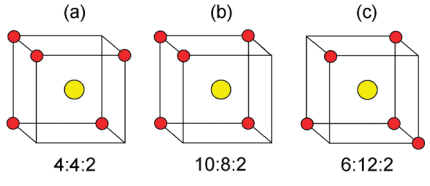

Figure 12. Models for oxide ion vacancy ordering of three vacancies in the idealized structure of δ-Bi_3YO_6, showing (a) ⟨111⟩ ⟨110⟩ ⟨100⟩, (b) ⟨100⟩ ⟨110⟩, and (c) ⟨110⟩⟨101⟩ ordering. Angle ratios for 70°, 109°, and 180° angles are given. Bi/Y and O are indicated by large yellow and small red circles, respectively.

listed in Table 6 and compared to the experimentally observed values. Interestingly, small differences in unit cell volume are observed for the different vacancy ordering configurations, with the ⟨110⟩ configuration yielding the largest unit cell volume of the ordered states, but still significantly lower than that for the disordered state.

Table 5. O−M−O Angle Ratios Derived from RMC Model of Bi_3YO_6

@ 25 °C		@ 800 °C	
angle (deg)	ratio	angle (deg)	ratio
71.44	6.0	72.78	5.0
107.99	8.0	106.28	9.1
180	2.0	180	2.0

Table 6. Calculated Lattice Energies and Calculated and Experimental Lattice Parameters for Different Vacancy Ordering Models in Bi_3YO_6

parameter	expt	Calc. ⟨100⟩	Calc. ⟨110⟩	Calc. ⟨111⟩	Calc. disordered
U_{latt} (eV)		−275.51	−275.71	−270.45	−275.49
volume (Å^3)	165.88	158.90	160.31	159.89	165.39
a (Å)	5.495	5.375	5.331	5.430	5.479
b (Å)	5.495	5.508	5.643	5.430	5.483
c (Å)	5.495	5.375	5.331	5.430	5.505
β (deg)	90.0	86.9	88.8	88.2	89.8

A significant feature of these supercell calculations is the observed relaxation of the O atoms from starting points equivalent to the 8*c* lattice position in the $Fm\bar{3}m$ subcell, to positions equivalent to the 32*f* site in the cubic subcell. The average deviation from the 8*c* lattice site was 0.47 Å. Therefore, the modeling work reproduces a structural feature observed in the experimental studies that was not incorporated into the input simulation structure and provides a valid starting point for the defect calculations.

The energies of isolated point defects (vacancies and interstitials) were calculated, with the possibility of oxygen vacancies on the various sites, as well as several possible interstitial sites. The most favorable interstitial site for oxide ions was found to be on the "intrinsic vacancy" sites at 8*c*. The 48*i* site was also considered for interstitial ions; however, the mean energy value was observed to be less favorable, by more than 1 eV. The total energies for Frenkel and Schottky-type disorder for the various species were then derived by combining the individual defect energies and the appropriate lattice energies according to the following reaction equations:

Oxygen Frenkel disorder:

$$O_O^{\times} \rightarrow V_O^{\bullet\bullet} + O_i'' \quad (3)$$

Bismuth Frenkel disorder:

$$Bi_{Bi}^{\times} \rightarrow V_{Bi}''' + Bi_i^{\bullet\bullet\bullet} \quad (4)$$

Bi_3YO_6 full Schottky disorder:

$$3Bi_{Bi}^{\times} + Y_Y^{\times} + 6O_O^{\times} \rightarrow 3V_{Bi}''' + V_Y''' + 6V_O^{\bullet\bullet} + Bi_3YO_6 \quad (5)$$

Bi_2O_3 partial Schottky disorder:

$$2Bi_{Bi}^{\times} + 3O_O^{\times} \rightarrow 2V_{Bi}''' + 3V_O^{\bullet\bullet} + Bi_2O_3 \quad (6)$$

Y_2O_3 partial Schottky disorder:

$$2Y_Y^{\times} + 3O_O^{\times} \rightarrow 2V_Y''' + 3V_O^{\bullet\bullet} + Y_2O_3 \quad (7)$$

The resulting defect formation energies are given in Table 7 and indicate two main features. First, the results

Table 7. Calculated Energies of Intrinsic Defects in Bi_3YO_6

defect	equation	defect energy (eV)
O Frenkel (8*c*)	3	0.54
O Frenkel (48*i*)	3	1.91
Bi Frenkel	4	25.93
Bi_3YO_6 Schottky	5	15.93
Bi_2O_3 partial Schottky	6	10.56
Y_2O_3 partial Schottky	7	11.60

suggest that cation Frenkel and all the Schottky-type defects are highly unlikely, which agrees well with experiment. Second, oxygen Frenkel disorder is clearly the most favorable intrinsic defect. This is consistent with our structural analysis, as well as a highly mobile oxygen sublattice in the Bi_3YO_6 system at higher temperatures.

5. Conclusions

The combination of a total scattering analysis and computer simulation is extremely powerful and appears to yield a more realistic description of the defect structure in disordered systems, which can be used to explain observed physical behavior. The analysis reveals detail of the local coordination environments around the cations, which is consistent with stereochemical activity of the Bi $6s^2$ nonbonding pair of electrons. The relatively poor neutron scattering contrast between Y and Bi results in difficulty in separating the scattering contributions of these atoms. The main advantage of this form of analysis over conventional Rietveld refinement appears to be the information on short-range ordering of vacancies.

Analysis of the angular distribution functions for Bi_3YO_6 shows, for the first time, physical evidence for predominantly ⟨110⟩ vacancy ordering in a bismuth oxide-based fluorite. Changes in the oxide ion distribution, which are a result of an increase in oxygen Frenkel defects, appear to be correlated to nonlinear behavior in the thermal expansion of the cubic lattice parameter, as well as Arrhenius plots of conductivity. A new interatomic potential model for Bi_3YO_6 has been developed in which the lowest energy vacancy-ordering model is found to be the ⟨110⟩ configuration. Defect calculations show that oxygen Frenkel disorder is the lowest energy intrinsic disorder, which is consistent with a highly mobile oxygen sublattice.

Acknowledgment. We gratefully acknowledge the Science and Technology Facilities Council (STFC) for a CMPC studentship grant to X.L. The authors thank the ISIS Facility for neutron beam time and Dr. R.M. Wilson for his help in X-ray data collection. M.S.I. and S.J.S. thank the Engineering and Physical Sciences Research Council (EPSRC) for their funding (EP/D077745/1) and Prof C. Greaves for useful discussions. S.T.N. wishes to thank Vetenskapsrådet (the Swedish Research Council) for financial support.